Contents lists available at ScienceDirect

Science of the Total Environment

Investigation of the migration of natural organic matter-iron-antimony nano-colloids in acid mine drainage

Yuqin Zhang [a], Pan Wu [a], Jian Zhu [a,*], Peng Liao [b,*], Elias Niyuhire [c], Feifei Fan [d], Wenjian Mao [a], Lisha Dong [a], Ruyi Zheng [a], Yi Li [e]

[a] College of Resources and Environmental Engineering, Key Laboratory of Karst Georesources and Environment, Guizhou Karst Environmental Ecosystems Observation and Research Station, Ministry of Education, Guizhou University, Guiyang 550025, China
[b] State Key Laboratory of Environmental Geochemistry, Institute of Geochemistry, Chinese Academy of Sciences, Guiyang 550081, China
[c] Ecole Normale Supérieure, Département des Sciences Naturelles, Centre de Recherche en Sciences et de Perfectionnement Professionnel, Boulevard Mwezi Gisabo, B.P.: 6983 Bujumbura, Burundi
[d] Guizhou Institute of Soil and Fertilizer, Guiyang 550006, China
[e] Guizhou Institute of Technology, Guiyang 550003, China

HIGHLIGHTS

- Natural organic matter influenced the formation of antimony colloids.
- Colloids play a significant role in acid mine drainage treatment.
- Colloids decreased with an increase in the C/Fe molar ratio.
- The transport of colloidal antimony is controlled by pH.

GRAPHICAL ABSTRACT
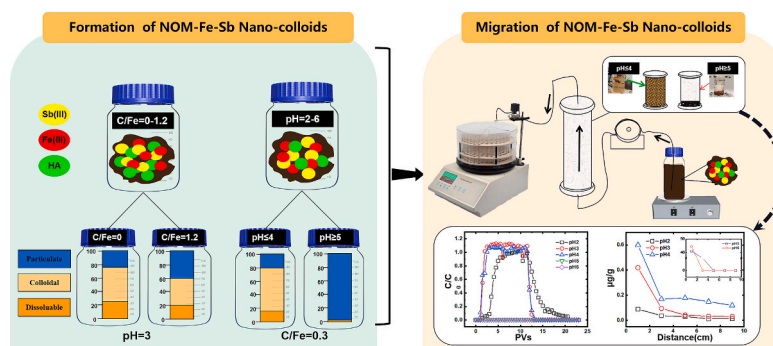
ARTICLE INFO

ABSTRACT

Colloids can potentially affect the efficacy of traditional acid mine drainage (AMD) treatment methods such as precipitation and filtration. However, it is unclear how colloids affect antimony (Sb) migration in AMD, especially when natural organic matter (NOM) is present. To conduct an in-depth investigation on the formation and migration behavior of NOM, iron (Fe), Sb and NOM-Fe-Sb colloids in AMD, experiments were performed under simulated AMD conditions. The results demonstrate significant variations in the formation of NOM-Fe-Sb colloids (1–3–450 nm) as the molar ratio of carbon to iron (C/Fe) increases within acidic conditions (pH = 3). Increasing the C/Fe molar ratio from 0.1 to 1.2 resulted in a decrease in colloid formation but an increase in particulate fraction. The distribution of colloidal Sb, Sb(III), and Fe(III) within the NOM-Fe-Sb colloids decreased from 68 % to 55 %, 72 % to 57 %, and 68 % to 55 %, respectively. Their distribution in the particulate fraction increased from 28 % to 42 %, 21 % to 34 %, and 8 % to 27 %. XRD, FTIR, and SEM-EDS analyses demonstrated that NOM facilitates the formation and crystallization of Fe_3O_4 and $FeSbO_4$ crystalline phases. The formation of the colloids

* Corresponding authors.
  E-mail addresses: Jzhu@gzu.edu.cn (J. Zhu), liaopeng@mail.gyig.ac.cn (P. Liao).

depended on pH. Our results indicate that NOM-Fe-Sb colloids can form when the pH ≤ 4, and the proportion of colloidal Sb fraction within the NOM-Fe-Sb colloids increased from 9 % to a maximum of 73 %. Column experiments show that the concentration of NOM-Fe-Sb colloids reaches its peak and remains stable at approximately 3.5 pore volumes (PVs), facilitating the migration of Sb in the porous media. At pH ≥ 5, stable NOM-Fe-Sb colloids do not form, and the proportion of colloidal Sb fraction decreases from 7 % to 0 %. This implies that as pH increases, the electrostatic repulsion between colloidal particles weakens, resulting in a reduction in the colloidal fraction and an increase in the particulate fraction. At higher pH values (pH ≥ 5), the repulsive forces between colloidal particles nearly disappear, promoting particle aggregation. The findings of this study provide important scientific evidence for understanding the migration behavior of NOM-Fe-Sb colloids in AMD. As the pH gradually shifts from acidic to near-neutral pH during the remediation process of AMD, these results could be applied to develop new strategies for this purpose.

1. Introduction

Acid mine drainage (AMD) is a significant environmental issue in the mining industry, resulting from the biogeochemical oxidation of iron-sulfide minerals exposed at the surface in ores and tailings (Bondu et al., 2023; Elghali et al., 2021). In AMD, there are high concentrations of heavy metal pollutants (e.g., Sb, Pb, Cu, Zn, Cd, among others) (Gao et al., 2019; Tang et al., 2020; Zhu et al., 2017) and microorganisms (Xu et al., 2020), along with natural organic matter (NOM) (Tang et al., 2020) generated from the decay of animals and plants. The interactions among these substances have a significant impact on the balance and stability of aquatic ecosystems.

Antimony (Sb), a highly toxic heavy metal found in AMD (Chen et al., 2023), has can migrate with the AMD flow and contaminate the surrounding ecological environment (Rastegari et al., 2022; Ren et al., 2023). With the increase in mining activities and industrial development, there is a growing concern about the process of Sb migration and transformation in the environment. Sb primarily exists in the natural environment in the forms of Sb(III) and Sb(V) (Wang et al., 2021; Zhu et al., 2018). Sb(III) is 10 times more toxic than Sb(V) and constitutes the main form of Sb at the outlet of mining-related AMD (Ferrari et al., 2023; Zhang et al., 2024). A previous research reported that the concentration of Sb in AMD can reach up to approximately 3160 μg/L (Zhou et al., 2017), causing a serious pollution to the environment.

In AMD, the formation of iron hydroxides can reduce the aqueous concentration of heavy metals, either through sorption, formation of surface precipitates, coprecipitation, or a combination of above three processes (Qu et al., 2022; Yang et al., 2022). In the natural evolution process of AMD, especially during periods of prolific planktonic reproduction, the content of NOM undergoes significant changes, resulting in AMD having abundant and dynamic carbon content (Kumar et al., 2016; Smucker et al., 2014). It has been reported that in the microbial ecology of highly acidic (pH = 1.8–2.3) underground environments, the concentration of NOM in many acidophilic habitats ranges from 3 to 24 mg/L (Johnson, 2012). NOM can affect the surface of Fe minerals formed in AMD. For example, a previous study showed that the adsorption of varied humic acid (HA) concentrations (i.e., 0.1–100 mg C/L) affected the surface charge of schwertmannite and goethite in AMD (Kumpulainen et al., 2008). Therefore, NOM plays a crucial role in the biogeochemical processes of Fe and heavy metals in AMD (Lazareva et al., 2019; Ouellet et al., 2013; Xia et al., 2023). NOM can exist in the form of dissolved, particulate, or colloidal forms (Artifon et al., 2019; Yao et al., 2020). Recent studies found that NOM can influence the particle stability of metals through complexation with metal ions, thereby affecting their migration (Li et al., 2022; Liao et al., 2020b).

Recent studies have recognized the pivotal role of colloids in the migration of pollutants in groundwater within mining areas (Jia et al., 2023). The presence of colloids could potentially affect the efficacy of traditional AMD treatment methods such as precipitation and filtration. Considering the unique characteristics of AMD, especially in the context of complex interactions between Fe, Sb, and NOM, the formation of colloids may play a more significant role in the mobility of Sb. Furthermore, during the remediation of AMD, contaminated groundwater gradually mixes with alkaline wastewater, leading to a shift from acidic to neutral pH. Whether the colloids could be formed during this process and how they could potentially impact the migration of Sb remain largely unknown. We hypothesize that by elucidating the intricate processes of colloid formation and migration in the complex interplay of Fe, Sb, and NOM, we can obtain new insights into the migration of Sb in AMD. Such insight might hold a paramount importance for enhancing and refining traditional AMD treatment methods.

The objective of this study was to investigate the formation and migration of NOM-Fe-Sb colloids in AMD. To this end, we (1) simulated the AMD conditions and conducted batch and column experiments under different C/Fe molar ratios and pH conditions; (2) analyzed the particle size and zeta potential of the colloids to understand their stability and charge characteristics; and (3) investigated the colloid structure, composition, and surface morphology using X-ray diffraction (XRD), Fourier transform infrared (FTIR), and scanning electron microscopy-Energy dispersive spectroscopy (SEM-EDS) to reveal their formation mechanisms and properties. Understanding the formation and migration of the colloids in AMD could facilitate the development of new wastewater treatment technologies and helps to protect the ecosystems and sustain water resources.

2. Materials and methods

2.1. Materials

All reagent solutions were prepared using ultrapure water (resistivity >18.2 MΩ·cm, Milli-Q, Millipore). A stock solution of Sb(III) was prepared by dissolving antimony trioxide (Sb_2O_3) (>99 %, Alfa Aesar) in 2 M HCl to reach a concentration of 50 mg/L. Similarly, ferric chloride hexahydrate ($FeCl_3 \cdot 6H_2O$, ≥99 %) was dissolved in 2 M HCl to obtain a 1000 mg/L Fe(III) stock solution.

Aldrich humic acid (HA, CAS: 1415-93-6) was obtained from Sigma-Aldrich. HA was selected because it is well-characterized and has been extensively used for NOM studies as a model NOM compound (Li et al., 2022; Li et al., 2019; Liao et al., 2017). A stock solution of HA was prepared by dissolving 2.5 g of solid HA in 500 mL of water and adjusting the pH to 10.5 with 1 M NaOH (Li et al., 2022). The mixture was stirred on a magnetic stirrer for 24 h in the dark and the resulting solution was filtered through 0.45 μm nitrocellulose filters (Millipore). The total organic carbon (TOC) in the HA stock suspensions was determined to be 1126 mg C/L using a TOC analyzer (Multi N/C 3100, Analytik Jena, Germany).

2.2. Batch experiments

All batch experiments were performed in 100 mL capped polypropylene bottles that were continuously stirred with Teflon-coated magnetic stir bars at 200 rpm and maintained at a constant temperature (25 ± 0.5 °C). To prepare a series of HA working solutions, appropriate volumes of HA stock solution were added into reaction vials and the pH was adjusted to 3 ± 0.2 (Huang et al., 2021). The final HA concentration of the working solutions ranged between 0 and 76.8 mg

C/L. These concentrations were selected because they are in the range of those occurring in the aquatic environments and are relevant in simulating the concentrations of NOM (0.1–100 mg C/L) found in AMD (Kumpulainen et al., 2008). Appropriate volumes of Fe(III) stock solution were gradually introduced into the reaction system to generate suspensions with varying C/Fe molar ratios (0–1.2). A suitable volume of Sb(III) stock solution was added into the reaction system to reach a final Sb(III) concentration of 0.5 mg/L. A thermostatic shaker operating at 200 rpm was used for the agitation of the reaction mixture. Following a 12 h equilibration period, a certain volume of each suspension with different C/Fe molar ratios was sampled and analyzed. Control experiments were conducted using HA and Fe(III) taken individually.

The experimental procedure for the formation of HA-Fe-Sb colloids under different pH conditions is similar to the colloid formation experiment under varying C/Fe molar ratio conditions. The distinction lies in the utilization of a solution with a C/Fe molar ratio of 0.3, wherein the pH is slowly adjusted from 2 to 6 using 1 M HCl/NaOH (Catrouillet et al., 2016).

2.3. Column experiments

The migration of HA-Fe-Sb colloids formed under different pH conditions was investigated through column experiments in a porous medium packed with quartz sand. Quartz sand with a median diameter of 0.50 mm was selected as the model porous medium. Prior to use, the sieved quartz sand (99.3 % SiO_2 with an average diameter of 0.4 mm) was soaked successively in 1 M HCl, 1 M NaOH, and 10 % H_2O_2 for 24 h separately to remove any metal oxides (Liao et al., 2020b). Subsequently, the quartz sand was rinsed many times with ultrapure water and was then dried at 85 °C in an oven for 24 h before use. Concentrations of 300 mg/L of Fe(III) and 19.2 mg C/L of HA were gradually introduced into a stirred Sb(III) solution of 500 mL. The pHs were adjusted to 2, 3, 4, 5, and 6 using 1 M HCl or NaOH, thereby obtaining HA-Fe-Sb influent suspensions under different pH conditions with a constant C/Fe molar ratio of 0.3. It is important to highlight that throughout the course of the column experiment, the influent suspension was continuously agitated using a stirrer, thereby ensuring the dispersion of the suspension. The specific procedure involves packing 84 g of purified quartz sand into a cylindrical organic glass column with a diameter of 2.6 cm × 10.5 cm, achieving a porosity of 0.44. Following the packing, a peristaltic pump is employed to upflow a background solution (high-purity water with varying pH levels) equivalent to approximately 10 pore volumes (PVs) through the column, aiming to establish a preliminary equilibration within the column. For all column experiments, a constant flow rate of 1 mL/min was maintained, corresponding to a Darcy velocity of approximately ~2.77 m/d.

Upon completion of the equilibration, samples of the column effluent were collected continuously from the outlet every 12 min using an automated fraction collector. Each column, in sequence, was exposed to HA-Fe-Sb suspensions with different pH values equivalent to 10 pore volumes (PVs), followed by elution using distinct pH background ultrapure water solutions equivalent to 13 PVs. Following the saturating step, 10 mg/L KBr were used in the column experiment as a conservative tracer. At the end of each column experiment, the retained Sb and Fe concentrations were determined. The sand grains were carefully excavated from the column under gravity in 2 cm increments (2 cm long for each segment) using 50 mL serum bottles. 20 mL of a 2 M HCl solution were added into each bottle. The bottles were vigorously shaken at 150 rpm overnight to ensure the complete dissolution and liberation of the retained Fe and Sb.

2.4. Chemical analysis

Samples collected at the equilibrium were analyzed for Sb, NOM and Fe concentrations in HA-Fe-Sb samples based on the following size fractionation: truly dissolved species (< 10 kDa, roughly equal to <1–3

nm), colloids (1–3 to 450 nm), and particulates (> 450 nm) (Li et al., 2019). Colloids were defined as particles ranging from 10 kDa to 450 nm (Liao et al., 2017). The concentrations of total Sb (Sb(T)) and Sb(III) in the supernatants or digested solution were analyzed using an atomic fluorescence spectrometer coupled with a hydride generator (HG-AFS, Beijing, China) with the detection limit of 0.1 μg/L (Yin et al., 2021). For the determination of Sb(T), samples were pretreated with an ascorbic acid/thiourea reducing agent (mixture of 5 % thiourea and 5 % ascorbic acid) to reduce all Sb to Sb(III) prior to hydride generation. Borohydride solution (2 g of KBH_4 in 100 mL of 0.5 % (w/v) NaOH solution) was used as reducing agent for SbH_3 generation and 5 % HCl solution was used as carrier solution. The HA concentration in each fraction was determined using a TOC analyzer. Dynamic light scattering (DLS) using a Zetasizer Nano (Zetasizer Nano, Malvern) was used to measure the particle size and zeta potential of the HA-Fe-Sb suspensions. The iron species introduced in this study is Fe(III). Therefore, the total Fe tested by atomic absorption spectrophotometry using a TAS-990 F instrument (Beijing Puxi General Instrument Co., Ltd.) represents the amount of Fe(III). Br^- concentrations were analyzed according to Geological and Mineral Industry standards of China (DZ/T 0064.46-2021). Briefly, 2 mL of water sample was added to a 25 mL colorimetric tube and adjusted to 10 mL with DI water. Subsequently, 0.5 mL of acetic acid-ammonium acetate buffer solution were added. Three drops of phenol red solution were then added with continuous shaking. Finally, 0.3 mL chloramine-T solution was added while shaking. The mixture was allowed to stand for 1 min, followed by the addition of 5 drops of sodium thiosulfate solution. The resulting mixture was diluted with pure water, and the absorbance was measured after 5 min using a 5 cm colorimetric cup at 590 nm in a spectrophotometer, with a reagent blank used as a reference.

2.5. Characterization of HA-Fe-Sb colloids

Solid samples of HA-Fe-Sb were centrifuged and freeze-dried. The surface properties of the resulting colloids were characterized by Fourier-transform infrared (FT-IR) spectroscopy (Thermo Fisher, Nicolet IS5). The mineralogy was evaluated using X-ray diffraction (XRD, Ultima IV, Japan). The morphology and composition of the sample were analyzed using scanning electron microscopy and energy-dispersive X-ray spectroscopy (SEM-EDS, EM-30, COXEM, Korea).

3. Results and discussion

3.1. Formation of NOM-Fe-Sb colloids

Under the pH conditions of 3 ± 0.2, the distribution percentages of Sb, Sb(III), Fe(III), and HA in the true dissolved form (<1–3 nm), colloidal form (1–3–450 nm), and particulate form (> 450 nm) within the HA-Fe-Sb mixed solutions reveal that the introduction of Fe(III) ions leads to the formation of colloidal particles (Fig. 1). The formation of HA-Fe-Sb colloids was significantly influenced by the C/Fe molar ratio. With increasing the C/Fe molar ratio from 0.1 to 1.2, the colloidal fraction was gradually reduced. The distribution of colloidal Sb, Sb(III), and Fe(III) in the NOM-Fe-Sb colloids decreased from 68 to 55 %, 72 to 57 %, and 68 to 55 %, respectively (Fig. 1 a-c). The distribution of particulate fraction increased from 28 to 42 %, 21 to 34 %, and 8 to 27 % (Fig. 1 a-c). In the presence of HA alone, colloidal HA was dominant (Fig. 1 d). With increasing the initial C/Fe molar ratio, colloidal HA decreased from 71 % to 54 % (Fig. 1 d). Simultaneously, the particle size of the HA-Fe-Sb colloids increased from 92.8 nm to 342.9 nm. Their formation was accompanied by the oxidation of Sb(III) to Sb (*V*) (Fig. 2 a and b). To further quantitatively probe the association between Fe(III) and HA during the process of colloids formation, we evaluated the ratio of the average stability constants for Fe(III) bound by truly soluble HA to that of Fe(III) bound by colloidal HA ($K_{Fe(III)-Sol.HA}$/ $K_{Fe(III)-Coll.HA}$) (Fig. 2 c) (Li et al., 2019; Wu et al., 2001). The ratios of $K_{Fe(III)-Sol.HA}$/ $K_{Fe(III)-Coll.HA}$ were < 1.0 when the initial C/Fe molar ratio exceeds 0.15, suggesting
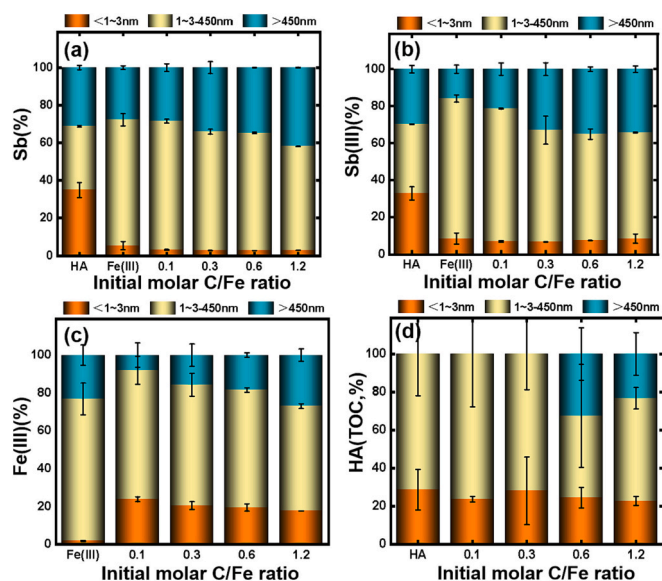
Fig. 1. Percentage of (a) Sb, (b) Sb(III), (c) Fe(III), and (d) HA concentrations in different size fractions as a function of the initial C/Fe molar ratios. The percentage on the y-axis represents the concentration of Sb, Sb(III), Fe(III), and HA in a certain size fraction relative to the total concentration of Sb, Sb(III), Fe(III), and HA in the suspension. The error bars represent the standard deviations of triplicate measurements. The size particle diameters of the dissolved, colloidal, and particulate form are <1–3 nm, 1–3–450 nm, and >450 nm, respectively.

that colloidal HA may have a high affinity for Fe(III) than truly soluble HA. At this C/Fe molar ratio, HA primarily forms colloidal complexes with Fe(III). This result is similar to the findings of Liao et al., showing that colloids composed of both HA and Fe(III) dominated at HA concentration > 5 mg C/L (Liao et al., 2020a).

The difference in the distribution of HA before and after reaction with Fe and Sb may be attributed to the interaction between HA and Fe and Sb. When only HA is present, HA-Sb colloidal complexes may form. For instance, HA combines with arsenic (As), forming colloidal complexes with diameters < 0.2 μm (Bauer and Blodau, 2009; Kar et al., 2011). Since Sb and As share similar chemical properties, the colloids formed in the presence of HA alone could potentially be composed of HA-Sb complexes. In the presence of iron alone, complexes of FeSbO$_4$ nanoparticles could be potentially formed (Tojo et al., 2008). The distribution of the dissolved forms remained nearly unchanged within the C/Fe range of 0.1 to 1.2, suggesting that the reduction in the colloidal form with increasing initial C/Fe molar ratio could be attributed to the increased transformation of the colloidal form into the particulate form. Compared to the case where Fe(III) existed alone, the increase of

dissolved Fe(III) is attributed to interaction between the acidic sites, mainly carboxyl groups, present in the HA. The introduction of HA enhances the solubility of iron (Whitby et al., 2020), leading to an increase in dissolved Fe(III). As the C/Fe molar ratio increases, organic functional groups such as COO- in HA form complexes with Fe(III), affecting the formation of the colloids. For instance, humic-like or fulvic acid substances could complex with Fe hydroxides and Sb to form DOM-Fe-Sb complexes or DOM-Sb complexes via ligand exchange mechanism (Hao et al., 2023). The oxidation of Sb(III) may be attributed to the oxidative properties exhibited by the organic functional groups in HA, which can act as oxidants in the oxidation reaction of Sb(III) (Wu et al., 2019). By increasing the C/Fe molar ratio, the concentrations of HA and organic functional groups are increased, which can lead to the increase in the oxidant concentration and facilitate the oxidation of Sb(III). HA molecules possess specific functional groups, such as aldehyde or ketone groups that possess strong redox properties and could oxidize Sb(III) (Buschmann et al., 2005; Wu et al., 2019). Although the colloid concentration steadily diminished, it remained predominant at all the C/Fe molar ratios. Additionally, HA could produce a higher adsorption affinity for Fe hydroxides surfaces, causing competition between Sb and NOM (Karimian et al., 2019), which may lower the free fraction of colloidal HA.

Qualitative distribution analyses suggest that the complexation of Sb and Fe by HA, coupled with the subsequent coagulation of HA macromolecular particles, played a pivotal role in the formation of HA-Fe-Sb colloids. The carbon moieties in HA can form complexes and coordination compounds with Fe and Sb. As the C/Fe ratio increases, the colloidal content decreases, and the particulate content increases (Fig. 1). Understanding the effective charge of colloidal particles is crucial to control the stability and performance of a colloidal system (Inam et al., 2019). With the increase in HA concentration, the ζ potential transitions from positive to negative (Fig. 5 a, b), indicating interactions among HA, Fe, and Sb. These interactions significantly influence the formation of colloids from NOM, Fe, and Sb. A good linear correlation observed among colloidal Sb, colloidal Fe(III), and colloidal HA served as robust confirmation of the colloidal interconnection between NOM, Fe(III), and Sb ($R^2 > 0.8$) (Fig. 3).

3.2. Formation of colloids under different pH conditions

During the AMD remediation process, the pH undergoes a gradual shift from acidic to neutral conditions (Martins et al., 2011). The formation of HA-Fe-Sb colloids is highly contingent upon pH regulation, wherein their abundance progressively decreases with increasing pH levels (pH = 3–6) (Fig. 4). At pH = 2, Sb, Sb(III), and Fe(III) predominantly exist in a dissolved form in the solution, with a relatively lower quantity of colloids formed with the organic matter. Specifically, the dissolved fraction of Sb, Sb(III), and Fe(III) accounts for 87 %, 52 %, and
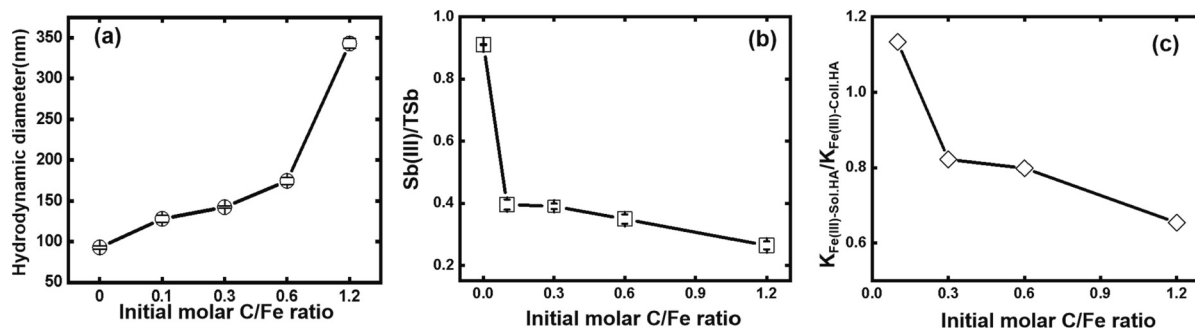

Fig. 2. (a) the particle size variations of the HA-Fe-Sb mixture under different initial C/Fe molar ratios, and (b) refers to the oxidation rate of Sb(III). (c) The evaluated $K_{Fe(III)-Sol.HA}$/ $K_{Fe(III)-Coll.HA}$ as a function of initial C/Fe molar ratios. $K_{Fe(III)-Sol.HA}$/$K_{Fe(III)-Coll.HA}$ = ([Sol. Fe(III)]/[Coll.Fe(III)]) × ([Coll. HA]/[Sol. HA]), where [Sol. Fe(III)] and [Coll. Fe(III)] are the truly soluble and colloidal Fe(III) concentration, respectively, [Sol. HA] and [Coll.HA] are the truly soluble and colloidal HA concentration, respectively.
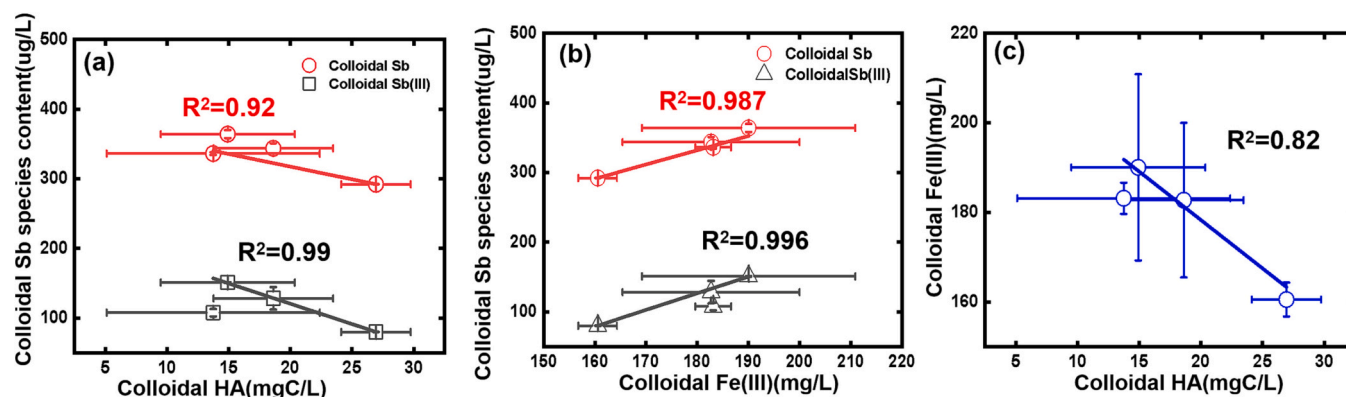
Fig. 3. Correlation between HA and Fe(III) and Sb species, and correlation between HA and Fe(III).
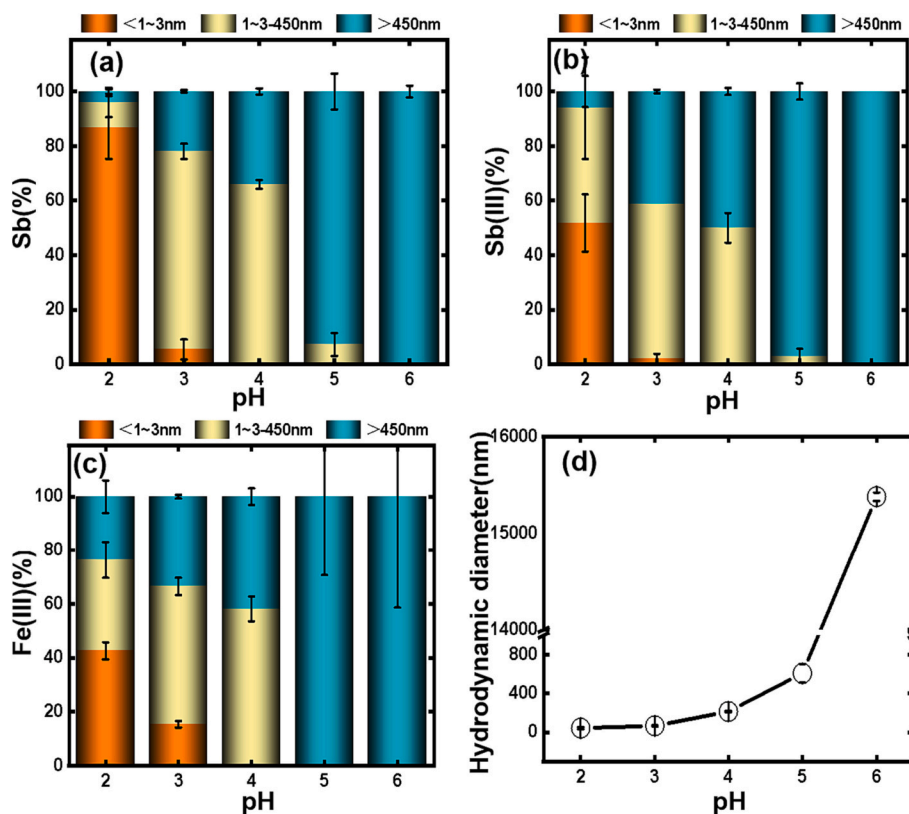

Fig. 4. Percentage of (a) Sb, (b) Sb(III), and (c) Fe(III) concentrations in different size fractions as a function of pH. The percentage on the y-axis represents the concentration of Sb, Sb(III), Fe(III), and HA in a certain size fraction relative to the total concentration of Sb, Sb(III), Fe(III), and HA in the suspension. (d) the particle size variations of the HA-Fe-Sb mixture under different pH.

43 % of the total concentrations, respectively, while the colloidal fraction represents 9 %, 42 %, and 34 % respectively (Fig. 4 a-c). The possible reason for this difference can be attributed to the acidic environment where Fe(III) and Sb(III) exist mainly in the dissolved form (Yang et al., 2020; Zhang et al., 2021). This leads to a weakened ability of metal ions to form complexes with organic matter, thereby limiting the formation of colloids. In contrast, Fe(III) and Sb(III) are more likely to form colloids. Fe(III) possesses higher charge and smaller ionic radius, which facilitate its formation of complexes or compounds with the organic matter. While Sb(III) can also form complexes or compounds with organic matter, it exhibits a comparatively lower tendency to form colloids compared to Fe(III).

However, as the pH of the solution gradually increases (pH ≤ 3), a gradual reduction in the colloid fraction and an increase in the

particulate fraction are observed. Specifically, within the pH range of 3 to 4, the solution is acidic, resulting a typical dissociation process of the carboxyl groups (Gustafsson et al., 2007). The carboxyl groups form complexes with Fe(III), reaching the point of zero charge (pzc) at a pH of about 3.6 (Fig. 5). Moreover, most HA-Fe-Sb colloidal particles acquire a positive charge (pH = 2–4). The positive charges create electrostatic repulsion, preventing the aggregation of colloidal particles and thus maintaining their colloidal form. During the shift from acidic to neutral pH, the ζ potential of HA is notably lower than under C/Fe molar ratio conditions (Fig. 5 c). This occurs because positively charged ions such as H^+ and Fe(III) neutralize the negatively charged functional groups in HA, thereby decreasing surface charge density under acidic conditions. When only HA is present, the ζ potential is lower than with the addition of Fe(III) (Fig. 5 a and b). However, as the pH of the mixed solution
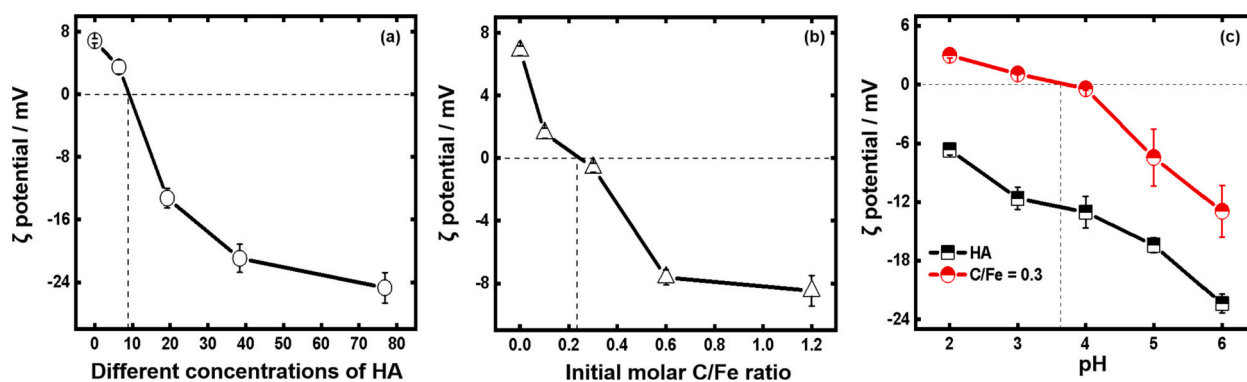
Fig. 5. (a) At different concentrations of humic acid (HA) (pH = 3 ± 0.1), (b) under various C/Fe molar ratios (pH = 3 ± 0.1), and (c) under different pH conditions, the zeta potential variations of humic acid and C/Fe molar ratio of 0.3 were investigated. Please note that the solutions all contained Sb(III) solution.

increases, the concentration of hydroxide ions (OH^-) in the solution also increases. The OH^- ions react with the positive charges on the surface of colloidal particles, leading to their neutralization, which weakens the electrostatic repulsion between the particles, facilitating their aggregation. Consequently, as the pH increases, the colloidal form gradually decreases while the particulate form increases.

When the pH > 4, the concentration of OH^- ions becomes sufficiently high to almost completely neutralize the positive charges on the surface of the colloidal particles. The elimination of positive charges removes the electrostatic repulsion between the colloidal particles, resulting in rapid particle aggregation. Therefore, at pH ≥ 5, the colloidal form is hardly observable, and the particulate form predominates. Additionally, the particle size also increases from ≈ 42 nm to ≈ 1537 nm with the pH (Fig. 4 d).

3.3. Characterization of HA-Fe-Sb colloids

SEM-EDS was used to characterize the morphology and elemental composition of the HA-Fe-Sb colloids (Fig. 6). At different pHs, different C/Fe molar ratios, and in the presence of Fe(III) alone, the colloids exhibit distinct morphological characteristics. In the presence of Fe(III) alone, it the colloids have a lamellar morphology with a relatively smooth surface and a potential compact structure under both acidic (pH = 3) and alkaline (pH = 6) conditions (Fig. 6 a). However, upon

introduction of HA, the edges of the complex become irregular, resulting in a rough and uneven surface, accompanied by partial particle aggregation (Fig. 6 b and c). This phenomenon is likely attributed to the presence of HA, which induces partial particle aggregation and contributes to the formation of the rugged features on the particle surface (Tan et al., 2019). Furthermore, with an increased C/Fe molar ratio, the surface becomes rougher and the degree of particle aggregation intensifies, potentially leading to the formation of larger aggregates or a continuous network structure (Fig. 6 b and c). This may be attributed to the stronger aggregation effect between HA and the Fe(III), particularly at higher C/Fe molar ratio, resulting in a rougher particle surface. Additionally, at pH = 6, a laminar morphology with a relatively smooth surface and a dense structure was observed (Fig. 6 d), suggesting that the particles remain intact without significant aggregation under these conditions. Meanwhile, the elemental analysis graph of the HA-Fe-Sb colloids clearly confirms the presence and content of C, Fe, and Sb (Fig. 6 b-d). As the C/Fe molar ratio increases, the elemental mass and atomic percentages within the HA-Fe-Sb complexes demonstrate varying degrees of change. This can be attributed to the introduction of a greater amount of HA through the increased C/Fe molar ratio, leading to a higher degree of complexation with Fe(III) and Sb. Thus, providing further evidence of the dispersed existence of C, Fe, and Sb and their interactions with HA. Moreover, at pH = 6 and C/Fe molar ratio of 0.3, there are minimal changes observed in the elements and their content
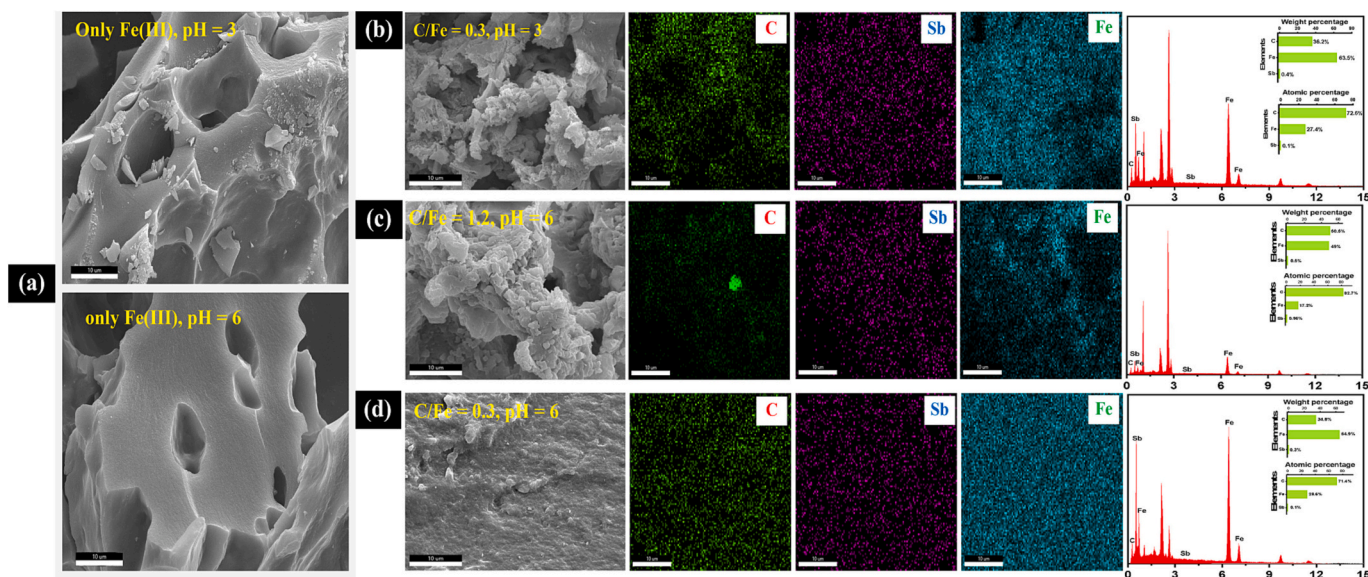

Fig. 6. SEM-EDS of HA-Fe-Sb particles formed under different conditions. (a) At pH 3 and pH 6, only Fe(III) is present, and there is no NOM. (b) under pH 3 with a C/Fe molar ratio of 0.3. (c) under a C/Fe molar ratio of 1.2 and pH 6. (d) under pH 6 with a C/Fe molar ratio of 0.3. The scale bar is 10 μm.

compared to pH = 3. This suggests that a relatively stable structure may have formed within the complex under these specific conditions. The coordination environment remains stable, and the complexation between HA, Fe(III), and Sb shows little variation. Consequently, the changes in the content of C, Fe, and Sb are relatively minor.

FTIR analysis revealed the presence and changes of specific functional groups in the HA, Fe, and Sb composite system. Three vibrational peaks associated with γ-FeOOH, Sb(III)-O, and Fe-O-Sb were observed at 1022 cm^{-1}, 690.5 cm^{-1}, and 465 cm^{-1}, respectively, under different C/Fe molar ratios (Fig. 7). In contrast, these peaks were not observed in the presence of Fe(III) alone. As the C/Fe molar ratio increases, the intensity of this coordination peak also increases. Coordination vibrations are caused by the coordination motion between metal ions and ligands. In this specific case, the formation of γ-FeOOH coordination bonds between Fe(III) and oxygen atoms in the HA leads to the observation of the γ-FeOOH coordination vibrational peak at 1022 cm^{-1}. A new peak appeared at 690.5 cm^{-1}, which is close to the peak observed at 690 cm^{-1} for the Sb$_2$O$_3$ (Xu et al., 2011). This suggests that this peak may be attributed to the stretching vibration of Sb(III)-O bonds. Furthermore, the presence of the Sb—O coordination vibrational peak at 690.5 cm^{-1} provides further evidence of the coordination interaction between Sb and oxygen atoms. However, the presence of Fe-O-Sb characteristic peak at 465 cm^{-1} suggests the possible interaction between Sb and iron (Zhang et al., 2019).

The enhanced peak intensity indicates that the coordination interaction between Fe(III) and oxygen atoms in the HA strengthens with an increasing C/Fe molar ratio, resulting in the intensification of coordination vibrations. Meanwhile, the transition of the solution environment from acidic (pH = 3) to neutral (pH = 6) is accompanied by a decrease in peak intensity. This can be attributed to the attenuation of the coordination interaction between Fe(III) and oxygen atoms in the HA under neutral conditions. pH variations can significantly influence the ionization degree and coordination capability of substances. In acidic conditions, the elevated concentration of hydrogen ions in the solution competes with Fe(III) ions for bonding sites, leading to a partial reduction in the formation of γ-FeOOH coordination bonds. As a result, higher intensities of coordination vibrational peaks are observed in acidic environments. However, as the solution environment becomes neutral and the pH increases, the decrease of H$^+$ concentration weakens the coordination interaction between Fe(III) ions and oxygen atoms in the HA. Consequently, the observed peak intensities of the coordination vibrational peaks decrease under neutral conditions, suggesting a lower extent of coordination bond formation. Additionally, characteristic peaks were observed at wavenumbers of 1622 cm^{-1}, 3392 cm^{-1} and 1386 cm^{-1} corresponding to the functional groups C=C/C=O, -OH and COO$^-$, respectively (Amir et al., 2010) (Fig. 7).

The XRD patterns reveal the presence of magnetite (Fe$_3$O$_4$) and Sb-based compound FeSbO$_4$ (Fig. 8), specifically with Sb existing in the Sb(V) oxidation state, upon introduction of HA to the system. The introduction of HA has been found to promote the formation and crystallization of Fe$_3$O$_4$ and FeSbO$_4$ phases, which is consistent with FTIR measurements. This indicates a substantial impact of HA on the structural evolution of HA-Fe-Sb colloids.

3.4. Migration of HA-Fe-Sb colloids

Column experiments were conducted under different pH conditions (Fig. 9). Breakthrough curves are plotted as normalized effluent concentrations (C/C$_0$) versus PVs, and retention profiles are plotted as solid-phase concentrations with distance from the column inlet. The penetration of Sb and Fe(III) closely approximates the penetration of a conservative tracer, i.e., bromide (~ 3 PVs) (Fig. 9 a). At pH ≥ 5, where no stable HA-Fe-Sb colloids formed, no breakthrough of Sb and Fe(III) occurs throughout the duration of the transport experiments (Fig. 9 b and c), as all injected HA-Fe-Sb particles are expected to be immobilized in the solid-phase. Retention profiles confirm that most Sb and Fe(III) are deposited adjacent to the column inlet (1–3 cm) and decreased hyper-exponentially with increasing depth (Fig. 9 d and e). In other words, the HA-Fe-Sb system exists in a particulate form at pH ≥ 5, and it is incapable of undergoing upward migration within a quartz sand column. However, other studies have found that the adjustment of experimental conditions such as pH, temperature, ion strength, and redox conditions may alter the stability of complexes (Liao et al., 2020a; Liu et al., 2023; Wei et al., 2021), prompting the re-dispersion of larger particles into smaller and potentially migratory particles (Zhang et al., 2022). Therefore, by changing environmental conditions, the stability of these particles may be disrupted, causing them to re-disperse and acquire the potential for migration.

Interestingly, HA-Fe-Sb colloids formed at pH ≤ 4 were mobile in the sand and remained stable to 11.5 PVs. However, at pH = 3 and pH = 4, the concentration of the HA-Fe-Sb colloids remained stable at approximately 3.5 PVs (C/C$_0$ ≥ 0.9), reaching its peak. The breakthrough of Sb and Fe(III) (~2 PVs) is close to the breakthrough of a conservative tracer (i.e., bromide), which occurred at ~2 PVs (Fig. 9 b). The shapes of breakthrough curves of Sb and Fe(III) particles are overall similar, but the plateau in the breakthrough curves of Sb was slightly higher than that of Fe(III) (e.g., C/C$_0$ = 1.0 to 1.1 versus 0.9 to 1.0, Fig. 9 b and c). The differential permeation behavior between pH = 2 and pH = 3 and 4 may be attributed to the variation in ion intensity under different pH conditions. This research reveals that under various pH conditions, changes in the concentrations of hydrogen ions (H$^+$) and hydroxide ions (OH$^-$) in the solution can alter the charge status of colloidal particle surfaces (Dong et al., 2016), which affects the stability of colloid aggregation. Retention profiles confirm that, when pH ≤ 4, HA-Fe-Sb migrates upward in a colloidal form within the glass column, and detectable levels of Sb and Fe(III) are measurable at the outlet (Fig. 9 d and e). When a colloid-free background solution (pH = 2–6) was introduced, almost all Sb and Fe(III) particles that had accumulated during the colloid injection step were eluted out of the column. The findings of this experiment further corroborate the predominance of colloidal forms in HA-Fe-Sb complexes formed at pH ≤ 4. This observation aligns with previous research findings, indicating that higher pH levels lead to an increase in particle size within the HA-Fe-Sb system. Therefore, under the same initial C/Fe molar ratio conditions, HA-Fe-Sb colloids exhibit distinct migration stability in different pH environments.

To further elucidate the migration behavior of HA-Fe-Sb colloids in quartz sand, FTIR measurements was conducted on quartz sand under
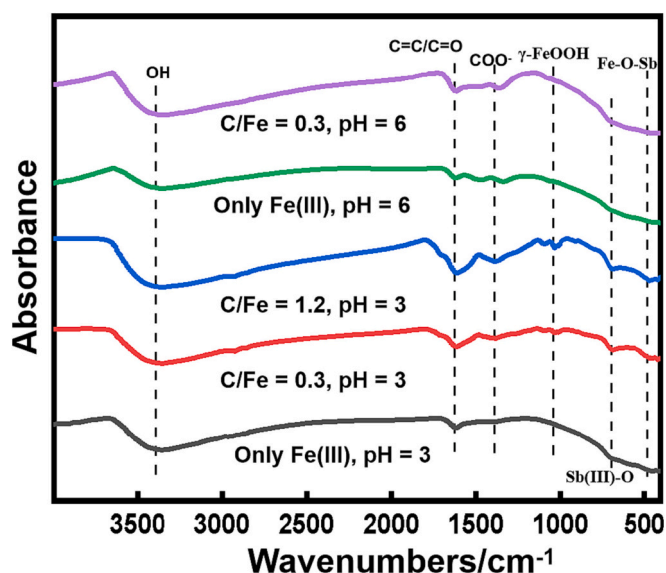

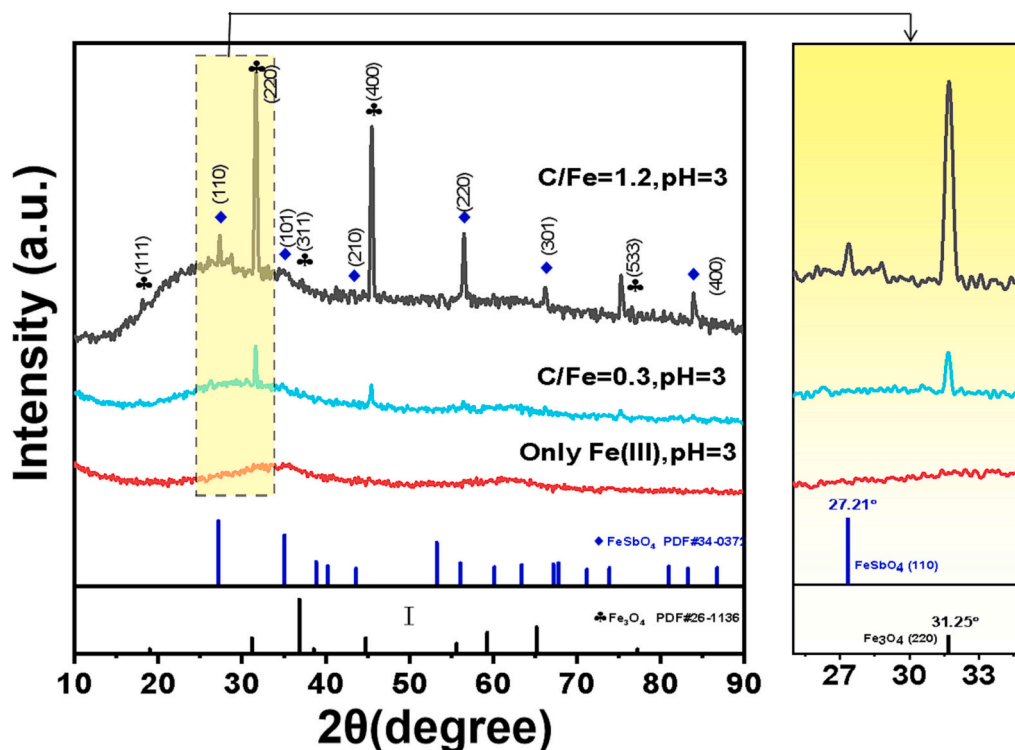**Fig. 7.** FTIR spectra of HA-Fe-Sb particles under different conditions.

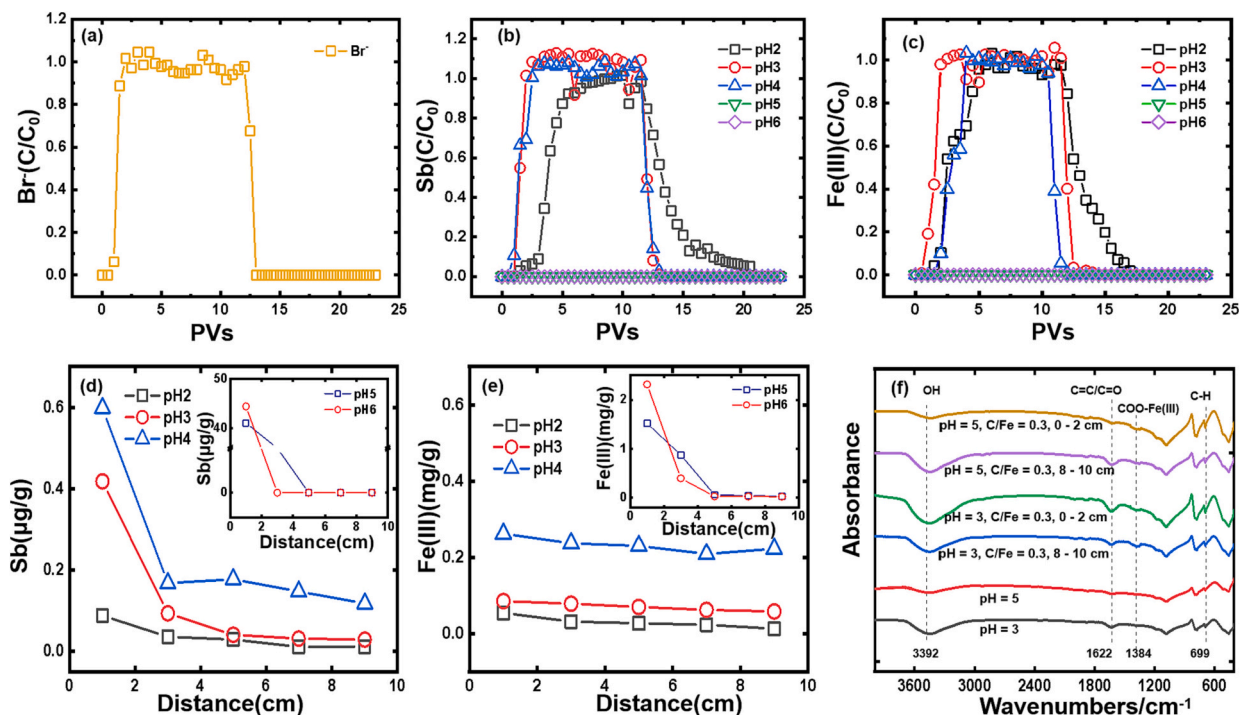**Fig. 8.** XRD analysis of HA-Fe-Sb particles under different conditions.

Fig. 9. The breakthrough curve of (a) the breakthrough curve of the tracer Br⁻, (b) Sb and (c) Fe(III) particles under different pH conditions (2, 3, 4, 5, 6). The retention curves of (d) Sb and (e) Fe(III) particles under different pH conditions (2, 3, 4, 5, 6). (f) The FTIR characterization of quartz sand under different conditions. The column experiment conditions are as follows: C/Fe molar ratio of 0.3, flow rate of 1 mL/min, pH values of 2, 3, 4, 5, 6, with an electrolyte solution of 5 mM NaCl.

different conditions (Fig. 9 f). The -OH, C=C/C=O, and C—H vibration peaks appear at 3392 cm^{-1}, 1622 cm^{-1}, and 699 cm^{-1} (Amir et al., 2010; Fang et al., 2010), respectively (Fig. 9 f). Moreover, at C/Fe molar ratio of 0.3, the peak intensity is significantly higher than that of quartz sand at pH = 3 and 5, suggesting that HA-Fe-Sb colloids may interact

with the surface of quartz sand, forming an adsorption layer, thereby altering the vibrational intensity of the quartz sand surface. At the same time, a new vibration peak COO-Fe (III) appears at 1384 cm^{-1}, consistent with previous reports (Li and Sun, 2011; Ou et al., 2009). This result indicates that during the interaction between HA-Fe-Sb colloids and

quartz sand, carboxyl groups bind to Fe(III), leading to the emergence of the COO-Fe(III) vibration peak.

4. Conclusion

This study aimed to elucidate the formation and migration processes of NOM-Fe-Sb colloids in AMD. Research indicates that the formation and migration of NOM-Fe-Sb colloids are strongly dependent on the concentration of HA and the chemical conditions of the solution. Under acidic conditions, the colloidal HA, Fe, and Sb decreases as the initial C/Fe molar ratio increases (C/Fe = 0–1.2). The electrostatic repulsion contributes to the stabilization of colloids, making them more likely to exist in the water column. Furthermore, the introduction of HA promotes the formation of Fe_3O_4 and $FeSbO_4$ phases to some extent, further affecting the formation and stability of the colloids. As the environmental conditions change from acidic (pH = 2) to neutral (pH = 6), significant alterations occur in the migration of NOM-Fe-Sb colloids. At pH $\leq$ 4, the formation of NOM-Fe-Sb colloids occurs, facilitating the transport of colloidal Sb. The breakthrough curve of NOM-Fe-Sb colloids peaks at approximately 3.5 PVs, with the HA-Fe complex migrating alongside Sb in colloidal form within quartz sand. However, at pH $\geq$ 5, larger NOM-Fe-Sb particles are formed, inhibiting the transport of Sb. These new findings can provide valuable insights for optimizing Sb remediation strategies and managing the environmental impact of AMD.

CRediT authorship contribution statement

Yuqin Zhang: Writing – original draft. **Pan Wu:** Conceptualization, Resources. **Jian Zhu:** Writing – review & editing, Resources. **Peng Liao:** Writing – review & editing. **Elias Niyuhire:** Writing – review & editing. **Feifei Fan:** Data curation. **Wenjian Mao:** Investigation. **Lisha Dong:** Investigation. **Ruyi Zheng:** Investigation. **Yi Li:** Investigation.

Declaration of competing interest

The authors declare that they have no known competing financial interests or personal relationships that could have appeared to influence the work reported in this paper.

Data availability

Data will be made available on request.

Acknowledgement

References

Amir, S., Jouraiphy, A., Meddich, A., El Gharous, M., Winterton, P., Hafidi, M., 2010. Structural study of humic acids during composting of activated sludge-green waste: elemental analysis, FTIR and 13C NMR. J. Hazard. Mater. 177 (1), 524–529.

Artifon, V., Zanardi-Lamardo, E., Fillmann, G., 2019. Aquatic organic matter: classification and interaction with organic microcontaminants. Sci. Total Environ. 649, 1620–1635.

Bauer, M., Blodau, C., 2009. Arsenic distribution in the dissolved, colloidal and particulate size fraction of experimental solutions rich in dissolved organic matter and ferric iron. Geochim. Cosmochim. Acta 73 (3), 529–542.

Bondu, R., Casiot, C., Pistre, S., Batiot-Guilhe, C., 2023. Impact of past mining activities on water quality in a karst area in the Cévennes region, Southern France. Sci. Total Environ. 873, 162274.

Buschmann, J., Canonica, S., Sigg, L., 2005. Photoinduced oxidation of antimony(III) in the presence of humic acid. Environ. Sci. Technol. 39 (14), 5335–5341.

Catrouillet, C., Davranche, M., Dia, A., Bouhnik-Le Coz, M., Demangeat, E., Gruau, G., 2016. Does As(III) interact with Fe(II), Fe(III) and organic matter through ternary complexes? J. Colloid Interface Sci. 470, 153–161.

Chen, H., Li, J., Dai, Z., Ai, Y., Jia, Y., Han, L., Zhang, W., Chen, M., 2023. In-situ immobilization of arsenic and antimony containing acid mine drainage through chemically forming layered double hydroxides. Sci. Total Environ. 903, 166601.

Dong, H., Ahmad, K., Zeng, G., Li, Z., Chen, G., He, Q., Xie, Y., Wu, Y., Zhao, F., Zeng, Y., 2016. Influence of fulvic acid on the colloidal stability and reactivity of nanoscale zero-valent iron. Environ. Pollut. 211, 363–369.

Elghali, A., Benzaazoua, M., Bouzahzah, H., Abdelmoula, M., Dynes, J.J., Jamieson, H.E., 2021. Role of secondary minerals in the acid generating potential of weathered mine tailings: crystal-chemistry characterization and closed mine site management involvement. Sci. Total Environ. 784, 147105.

Fang, J., Xuan, Y., Li, Q., 2010. Preparation of polystyrene spheres in different particle sizes and assembly of the PS colloidal crystals. SCIENCE CHINA Technol. Sci. 53 (11), 3088–3093.

Ferrari, C., Resongles, E., Héry, M., Désoeuvre, A., Freydier, R., Delpoux, S., Bruneel, O., Casiot, C., 2023. Antimony isotopic fractionation during Sb(III) oxidation to Sb(V): biotic and abiotic processes. Chem. Geol. 641, 121788.

Gao, K., Jiang, M., Guo, C., Zeng, Y., Fan, C., Zhang, J., Reinfelder, J.R., Huang, W., Lu, G., Dang, Z., 2019. Reductive dissolution of jarosite by a sulfate reducing bacterial community: secondary mineralization and microflora development. Sci. Total Environ. 690, 1100–1109.

Gustafsson, J.P., Persson, I., Kleja, D.B., van Schaik, J.W.J., 2007. Binding of Iron(III) to organic soils: EXAFS spectroscopy and chemical equilibrium modeling. Environ. Sci. Technol. 41 (4), 1232–1237.

Hao, C., Sun, X., Peng, Y., Xie, B., He, K., Wang, Y., Liu, M., Fan, X., 2023. Geochemical impact of dissolved organic matter on antimony mobilization in shallow groundwater of the Xikuangshan antimony mine, Hunan Province, China. Sci. Total Environ. 860, 160292.

Huang, Y., Li, X.-T., Jiang, Z., Liang, Z.-L., Wang, P., Liu, Z.-H., Li, L.-Z., Yin, H.-Q., Jia, Y., Huang, Z.-S., Liu, S.-J., Jiang, C.-Y., 2021. Key factors governing microbial community in extremely acidic mine drainage (pH < 3). Front. Microbiol. 12, 761579.

Inam, M.A., Khan, R., Park, D.R., Khan, S., Uddin, A., Yeom, I.T., 2019. Complexation of antimony with natural organic matter: performance evaluation during coagulation-flocculation process. Int. J. Environ. Res. Public Health 16 (7), 1092.

Jia, X., Majzlan, J., Ma, L., Liu, P., Fan, P., Li, W., Zhou, J., Wen, B., 2023. Novel insights into the mechanisms for Sb mobilization in groundwater in a mining area: a colloid field study. J. Hazard. Mater. 459, 132212.

Johnson, D.B., 2012. Geomicrobiology of extremely acidic subsurface environments. FEMS Microbiol. Ecol. 2 (67), 1145–1156.

Kar, S., Maity, J.P., Jean, J.-S., Liu, C.-C., Nath, B., Lee, Y.-C., Bundschuh, J., Chen, C.-Y., Li, Z., 2011. Role of organic matter and humic substances in the binding and mobility of arsenic in a Gangetic aquifer. J. Environ. Sci. Health A 46 (11), 1231–1238.

Karimian, N., Burton, E.D., Johnston, S.G., 2019. Antimony speciation and mobility during Fe(II)-induced transformation of humic acid-antimony(V)-iron(III) coprecipitates. Environ. Pollut. 254, 113112.

Kumar, R.N., McCullough, C.D., Lund, M.A., Larranaga, S.A., 2016. Assessment of factors limiting algal growth in acidic pit lakes—a case study from Western Australia, Australia. Environ. Sci. Pollut. Res. 23 (6), 5915–5924.

Kumpulainen, S., von der Kammer, F., Hofmann, T., 2008. Humic acid adsorption and surface charge effects on schwertmannite and goethite in acid sulphate waters. Water Res. 42 (8), 2051–2060.

Lazareva, E.V., Myagkaya, I.N., Kirichenko, I.S., Gustaytis, M.A., Zhmodik, S.M., 2019. Interaction of natural organic matter with acid mine drainage: in-situ accumulation of elements. Sci. Total Environ. 660, 468–483.

Li, S., Sun, W., 2011. A comparative study on aggregation/sedimentation of TiO2 nanoparticles in mono- and binary systems of fulvic acids and Fe(III). J. Hazard. Mater. 197, 70–79.

Li, Q., Xie, L., Jiang, Y., Fortner, J.D., Yu, K., Liao, P., Liu, C., 2019. Formation and stability of NOM-Mn(III) colloids in aquatic environments. Water Res. 149, 190–201.

Li, B., Liao, P., Liu, P., Wang, D., Ye, Z., Wang, J., Chen, J., Ning, Z., Jiang, Y., Liu, C., 2022. Formation, aggregation, and transport of NOM–Cr(III) colloids in aquatic environments. Environ. Sci. Nano 9 (3), 1133–1145.

Liao, P., Li, W., Jiang, Y., Wu, J., Yuan, S., Fortner, J.D., Giammar, D.E., 2017. Formation, aggregation, and deposition dynamics of nom-iron colloids at anoxic–oxic interfaces. Environ. Sci. Technol. 51 (21), 12235–12245.

Liao, P., Pan, C., Ding, W., Li, W., Yuan, S., Fortner, J.D., Giammar, D.E., 2020a. Formation and Transport of Cr(III)-NOM-Fe Colloids upon Reaction of Cr(VI) with NOM-Fe(II) Colloids at Anoxic–Oxic Interfaces. Environ. Sci. Technol. 54 (7), 4256–4266.

Liao, P., Pan, C., Ding, W., Li, W., Yuan, S., Fortner, J.D., Giammar, D.E.J.E.S., Technology, 2020b. Formation and transport of Cr (III)-NOM-Fe colloids upon reaction of Cr (VI) with NOM-Fe (II) colloids at anoxic–oxic interfaces. Environ. Sci. Technol. 54 (7), 4256–4266.

Liu, B., Guo, C., Ke, C., Chen, K., Dang, Z., 2023. Colloidal stability and aggregation behavior of CdS colloids in aquatic systems: effects of macromolecules, cations, and pH. Sci. Total Environ. 869, 161814.

Martins, M., Santos, E.S., Faleiro, M.L., Chaves, S., Tenreiro, R., Barros, R.J., Barreiros, A., Costa, M.C., 2011. Performance and bacterial community shifts during bioremediation of acid mine drainage from two Portuguese mines. Int. Biodeterior. Biodegradation 65 (7), 972–981.

Ou, X., Chen, S., Quan, X., Zhao, H., 2009. Photochemical activity and characterization of the complex of humic acids with iron(III). J. Geochem. Explor. 102 (2), 49–55.

Ouellet, J.D., Dubé, M.G., Niyogi, S., 2013. Influence of elevated alkalinity and natural organic matter (NOM) on tissue-specific metal accumulation and reproductive performance in fathead minnows during chronic, multi-trophic exposures to a metal mine effluent. Ecotoxicol. Environ. Saf. 95, 104–112.

Qu, C., Chen, J., Mortimer, M., Wu, Y., Cai, P., Huang, Q., 2022. Humic acids restrict the transformation and the stabilization of Cd by iron (hydr)oxides. J. Hazard. Mater. 430, 128365.

Rastegari, M., Karimian, N., Johnston, S.G., Doherty, S.J., Hamilton, J.L., Choppala, G., Hosseinpour Moghaddam, M., Burton, E.D., 2022. Antimony(V) incorporation into Schwertmannite: critical insights on antimony retention in acidic environments. Environ. Sci. Technol. 56 (24), 17776–17784.

Ren, W., Ran, Y., Mou, Y., Cui, Y., Sun, B., Yu, L., Wan, D., Hu, D., Zhao, P., 2023. Pollution characteristics and risk assessment of antimony and arsenic in a typical abandoned antimony smelter. Environ. Geochem. Health 45 (7), 5467–5480.

Smucker, N.J., Drerup, S.A., Vis, M.L., 2014. Roles of benthic algae in the structure, function, and assessment of stream ecosystems affected by acid mine drainage. J. Phycol. 50 (3), 425–436.

Tan, L., Yu, Z., Tan, X., Fang, M., Wang, X., Wang, J., Xing, J., Ai, Y., Wang, X., 2019. Systematic studies on the binding of metal ions in aggregates of humic acid: aggregation kinetics, spectroscopic analyses and MD simulations. Environ. Pollut. 246, 999–1007.

Tang, Y., Xie, Y., Lu, G., Ye, H., Dang, Z., Wen, Z., Tao, X., Xie, C., Yi, X., 2020. Arsenic behavior during gallic acid-induced redox transformation of jarosite under acidic conditions. Chemosphere 255, 126938.

Tojo, T., Zhang, Q., Saito, F., 2008. Mechanochemical synthesis of FeSbO4-based materials from FeOOH and Sb2O5 powders. Powder Technol. 181 (3), 281–284.

Wang, A., He, M., Ouyang, W., Lin, C., Liu, X., 2021. Effects of antimony (III/V) on microbial activities and bacterial community structure in soil. Sci. Total Environ. 789, 148073.

Wei, X., Pan, D., Xu, Z., Xian, D., Li, X., Tan, Z., Liu, C., Wu, W., 2021. Colloidal stability and correlated migration of illite in the aquatic environment: the roles of pH, temperature, multiple cations and humic acid. Sci. Total Environ. 768, 144174.

Whitby, H., Planquette, H., Cassar, N., Bucciarelli, E., Osburn, C.L., Janssen, D.J., Cullen, J.T., González, A.G., Völker, C., Sarthou, G., 2020. A call for refining the role of humic-like substances in the oceanic iron cycle. Sci. Rep. 10 (1), 6144.

Wu, J., Boyle, E., Sunda, W., Wen, L.-S., 2001. Soluble and colloidal iron in the oligotrophic North Atlantic and North Pacific. Science 293 (5531), 847–849.

Wu, T.-l., Qin, W.-x., Alves, M.E., Fang, G.-d., Sun, Q., Cui, P.-x., Liu, C., Zhou, D.-m., Wang, Y.-j., 2019. Mechanisms of Sb(III) oxidation mediated by low molecular weight phenolic acids. Chem. Eng. J. 356, 190–198.

Xia, S., Song, Z., Zhao, X., Li, J., 2023. Review of the recent advances in the prevention, treatment, and resource recovery of acid mine wastewater discharged in coal mines. J. Water Process Eng. 52, 103555.

Xu, W., Wang, H., Liu, R., Zhao, X., Qu, J., 2011. The mechanism of antimony(III) removal and its reactions on the surfaces of Fe–Mn Binary Oxide. J. Colloid Interface Sci. 363 (1), 320–326.

Xu, R., Li, B., Xiao, E., Young, L.Y., Sun, X., Kong, T., Dong, Y., Wang, Q., Yang, Z., Chen, L., Sun, W., 2020. Uncovering microbial responses to sharp geochemical gradients in a terrace contaminated by acid mine drainage. Environ. Pollut. 261, 114226.

Yang, Y., Chen, S., Wang, B., Wen, X., Li, H., Zeng, R.J., 2020. Effect of ferric ions on the anaerobic bio-dissolution of jarosites by Acidithiobacillus ferrooxidans. Sci. Total Environ. 710, 136334.

Yang, Z., Ma, J., Liu, F., Zhang, H., Ma, X., He, D., 2022. Mechanistic insight into pH-dependent adsorption and coprecipitation of chelated heavy metals by in-situ formed iron (oxy)hydroxides. J. Colloid Interface Sci. 608, 864–872.

Yao, Y., Mi, N., He, C., Yin, L., Zhou, D., Zhang, Y., Sun, H., Yang, S., Li, S., He, H., 2020. Transport of arsenic loaded by ferric humate colloid in saturated porous media. Chemosphere 240, 124987.

Yin, X., Zhang, G., Su, R., Zeng, X., Yan, Z., Zhang, D., Ma, X., Lei, L., Lin, J., Wang, S., Jia, Y., 2021. Oxidation and incorporation of adsorbed antimonite during iron(II)-catalyzed recrystallization of ferrihydrite. Sci. Total Environ. 778, 146424.

Zhang, C., Jiang, H., Deng, Y., Wang, A.J.R.a., 2019. Adsorption performance of antimony by modified iron powder. RSC Adv. 9 (54), 31645–31653.

Zhang, Y., Ding, C., Gong, D., Deng, Y., Huang, Y., Zheng, J., Xiong, S., Tang, R., Wang, Y., Su, L., 2021. A review of the environmental chemical behavior, detection and treatment of antimony. Environ. Technol. Innov. 24, 102026.

Zhang, D., Wang, Y., Heng, J., Diao, X., Zu, G., Jin, Q., Chen, Z., Guo, Z., 2022. Stability of Eu(III)-silicate colloids: effect of Eu content, pH, electrolyte and fulvic acid. J. Hazard. Mater. 438, 129363.

Zhang, Z., Boyanov, M.I., O'Loughlin, E.J., Kemner, K.M., Sanford, R.A., Kim, H.-S., Park, S.-C., Kwon, M.J., 2024. Reaction pathways and Sb(III) minerals formation during the reduction of Sb(V) by Rhodoferax ferrireducens strain YZ-1. J. Hazard. Mater. 465, 133240.

Zhou, J., Nyirenda, M.T., Xie, L., Li, Y., Zhou, B., Zhu, Y., Liu, H., 2017. Mine waste acidic potential and distribution of antimony and arsenic in waters of the Xikuangshan mine, China. Appl. Geochem. 77, 52–61.

Zhu, J., Zhang, P., Yuan, S., Liao, P., Qian, A., Liu, X., Tong, M., Li, L., 2017. Production of hydroxyl radicals from oxygenation of simulated AMD due to CaCO3-induced pH increase. Water Res. 111, 118–126.

Zhu, Y., Wu, M., Gao, N., Chu, W., An, N., Wang, Q., Wang, S., 2018. Removal of antimonate from wastewater by dissimilatory bacterial reduction: role of the coexisting sulfate. J. Hazard. Mater. 341, 36–45.